EXTENDED PDF FORMAT
SPONSORED BY

BIO-RAD

http://discover.bio-rad.com



Control of Crystal Size and Lattice Formation by Starmaker in Otolith Biomineralization

Christian Söllner, *et al.*

Science **302**, 282 (2003);
DOI: 10.1126/science.1088443

The following resources related to this article are available online at www.sciencemag.org (this information is current as of January 2, 2007):

Updated information and services, including high-resolution figures, can be found in the online version of this article at:
http://www.sciencemag.org/cgi/content/full/302/5643/282

Supporting Online Material can be found at:
http://www.sciencemag.org/cgi/content/full/302/5643/282/DC1

A list of selected additional articles on the Science Web sites **related to this article** can be found at:
http://www.sciencemag.org/cgi/content/full/302/5643/282#related-content

This article **cites 19 articles**, 8 of which can be accessed for free:
http://www.sciencemag.org/cgi/content/full/302/5643/282#otherarticles

This article has been **cited by** 37 article(s) on the ISI Web of Science.

This article has been **cited by** 4 articles hosted by HighWire Press; see:
http://www.sciencemag.org/cgi/content/full/302/5643/282#otherarticles

This article appears in the following **subject collections**:
Development
http://www.sciencemag.org/cgi/collection/development

Information about obtaining **reprints** of this article or about obtaining **permission to reproduce this article** in whole or in part can be found at:
http://www.sciencemag.org/help/about/permissions.dtl

Downloaded from www.sciencemag.org on January 2, 2007

Science (print ISSN 0036-8075; online ISSN 1095-9203) is published weekly, except the last week in December, by the American Association for the Advancement of Science, 1200 New York Avenue NW, Washington, DC 20005. Copyright c 2006 by the American Association for the Advancement of Science; all rights reserved. The title SCIENCE is a registered trademark of AAAS.

formation during cycling of the spliceosome (*21*, *23*). Our finding that Lsm proteins became loosely associated with the active spliceosome further demonstrated a dynamic association of Lsm proteins with U6 and a direct role for Lsm in spliceosome activation. Thus, despite structural similarity, Lsm proteins may play distinct roles from Sm proteins in the splicing reaction, not only being involved in the assembly of U6 or U4/U6 snRNP but also actively participating in the conformational rearrangement of the spliceosome during its activation.

In this report, we show that NTC was not required for dissociation of U4 but was required for subsequent stabilization of U5 and U6 on the spliceosome. Stabilization of U6 involved remodeling of interactions between U6 and the pre-mRNA, including a switch of base pairings between U6 and the 5′ splice site and the formation of new interactions between the 3′ terminal U-tract of U6 and the intron sequence near the 5′ splice site. The latter interaction might require destabilization of Lsm proteins from U6 to expose its 3′ terminal sequence. In this view, NTC may be involved in multiple steps of structural rearrangement of the spliceosome. At least eight proteins have been identified as components of NTC (*8*–*11*), and several others are possible candidates for NTC components from recent proteomic analyses of the spliceosome and NTC-related complexes (*24*–*28*). Whether different NTC components function in mediating different aspects of structural change or the entire complex functions as a whole to catalyze all the structural rearrangements remains to be studied.

References and Notes

1. C. B. Burge, T. H. Tuschl, P. A. Sharp, in *RNA World II*, R. F. Gesteland, T. R. Cech, and J. F. Atkins, Eds. (Cold Spring Harbor Laboratory Press, Cold Spring Harbor, NY, 1999) pp. 525–560.
2. C. L. Will, R. Lührmann, *Curr. Opin. Cell Biol.* **9**, 320 (1997).
3. D. A. Brow, *Annu. Rev. Genet.* **36**, 333 (2002).
4. P. L. Raghunathan, C. Guthrie, *Curr. Biol.* **8**, 847 (1998).
5. J. P. Staley, C. Guthrie, *Mol. Cell* **3**, 55 (1999).
6. J. Y.-F. Chen *et al.*, *Mol. Cell* **7**, 227 (2001).
7. W.-Y. Tarn *et al.*, *EMBO J.* **13**, 2421 (1994).
8. W.-Y. Tsai *et al.*, *J. Biol. Chem.* **274**, 9455 (1999).
9. C.-H. Chen, W.-Y. Tsai, H.-R. Chen, C.-H. Wang, S.-C. Cheng, *J. Biol. Chem.* **276**, 488 (2001).
10. H.-R. Chen *et al.*, *Mol. Cell. Biol.* **18**, 2196 (1998).
11. C.-H. Chen *et al.*, *Nucl. Acids Res.* **30**, 1029 (2002).
12. W.-Y. Tarn, K.-R. Lee, S.-C. Cheng, *Mol. Cell. Biol.* **13**, 1883 (1993).
13. W.-Y. Tarn, K.-R. Lee, S.-C. Cheng, *Proc. Natl. Acad. Sci. U.S.A.* **90**, 10821 (1993).
14. U. Vijayraghavan *et al.*, *EMBO J.* **5**, 1683 (1986).
15. S.-C. Cheng, *Nucleic Acids Res.* **22**, 1548 (1994).
16. H. Sawa, Y. Shimura, *Genes Dev.* **6**, 244 (1992).
17. H. Sawa, J. Abelson, *Proc. Natl. Acad. Sci. U.S.A.* **89**, 11269 (1992).
18. C. F. Lesser, C. Guthrie, *Science* **262**, 1982 (1993).
19. E. J. Sontheimer, J. A. Steitz, *Science* **262**, 1989 (1993).
20. C. H. Kim, J. Abelson, *RNA* **2**, 995 (1996).
21. T. Achsel *et al.*, *EMBO J.* **18**, 5789 (1999).
22. B. Séraphin, *EMBO J.* **14**, 2089 (1995).
23. A. E. Mayes, L. Verdone, P. Legrain, J. D. Beggs, *EMBO J.* **18**, 4321 (1999).
24. Q. Wang, K. Hobbs, B. Lynn, B. C. Rymond, *J. Biol. Chem.* **278**, 7875 (2003).
25. M. D. Ohi *et al.*, *Mol. Cell. Biol.* **22**, 2011 (2002).
26. P. Ajuh *et al.*, *EMBO J.* **19**, 6569 (2000).
27. Z. Zhou, L. J. Licklider, S. P. Gygi, R. Reed, *Nature* **419**, 182 (2002).
28. E. M. Makarov *et al.*, *Science* **298**, 2205 (2002).

29. We thank C. Guthrie, J. Abelson, S. Radar, D. Ryan, and D. Brow for critical reading of the manuscript and K. J. Deen for English editing. This work was supported by a grant from the Academia Sinica and by National Science Council (Taiwan) NSC91-2321-B-001-014.

Supporting Online Material

www.sciencemag.org/cgi/content/full/1086602/DC1
Materials and Methods
References

8 May 2003; accepted 4 August 2003
Published online 11 September 2003;
10.1126/science.1086602
Include this information when citing this paper.

Control of Crystal Size and Lattice Formation by Starmaker in Otolith Biomineralization

Christian Söllner,[1] Manfred Burghammer,[3] Elisabeth Busch-Nentwich,[1] Jürgen Berger,[2] Heinz Schwarz,[2] Christian Riekel,[3] Teresa Nicolson[1]*†

The stone-like otoliths from the ears of teleost fishes are involved in balance and hearing and consist of calcium carbonate crystallites embedded in a protein framework. We report that a previously unknown gene, *starmaker*, is required in zebrafish for otolith morphogenesis. Reduction of *starmaker* activity by injection of modified antisense oligonucleotides causes a change in the crystal lattice structure and thus a change in otolith morphology. The expression pattern of *starmaker*, along with the presence of the protein on the growing otolith, suggest that the expression levels of *starmaker* control the shape of the otoliths.

Biologically formed crystals differ from their inorganic counterparts by protein-mediated control of their shape, size, and crystallographic axes orientation (*1*, *2*). Fish otoliths are such calcified biominerals, composed of the calcium carbonate polymorph aragonite and a small fraction of organic molecules, including proteoglycans and glycoproteins (*3*, *4*). Otoliths are present in the inner ear, where they act as an inertial mass on the otolithic membrane, thereby enhancing the sensitivity of the underlying sensory epithelium to gravitational and linear acceleration forces. In addition to the perception of balance, otoliths are involved in the reception of sound (*5*, *6*).

Higher vertebrates have biomineralized structures in their inner ears called otoconia. Several genes involved in their biogenesis have been identified. Among them are the acidic glycoproteins, Otoconins, which share homology with secretory phospholipase A2 (*7*–*9*); Pendrin, an anion transporter (*10*); and Otopetrin 1, a protein with 10 transmembrane domains (*11*). Disruption of their function leads to a complete loss of otoconia or, in rare cases, to the formation of giant otoconia.

Mutations in the human dentin sialophosphoprotein gene (*DSPP*) are responsible for dentinogenesis imperfecta and can be associated with hearing loss (*12*, *13*). Because *DSPP* is required for mineralization of the teeth and is expressed in the ear (*14*), we postulated that homologous genes in zebrafish might mediate otolith formation. By searching zebrafish cDNA libraries for *dspp*-like or related genes from ear tissues, we identified the zebrafish gene *starmaker*. It is similar to *DSPP* in that it encodes a protein with many acidic residues; however, the overall structure of the gene is different, including sequences encoding additional N-terminal repeats. *starmaker* encodes a 613–amino acid protein with a predicted signal peptide at the N terminus and four highly conserved internal repeats, each encoded by a single exon (Fig. 1, A and B). The function of the internal repeats is not known. With the exception of the signal peptide, the Starmaker protein is extremely hydrophilic. The program NetPhos (*15*) predicts that 20% of the residues could be phosphorylated (112 serines and 16 tyrosines). One large exon (623 base pairs) encodes mainly alternating serines and aspartic acids for a stretch of 60 residues. In total, 35% of Starmaker is composed of acidic residues.

[1]Max Planck Institut für Entwicklungsbiologie, [2]Microscopy Unit, Max Planck Institut für Entwicklungsbiologie, Spemannstrasse 35, 72076 Tübingen, Germany. [3]European Synchrotron Radiation Facility, Post Office Box 220, F–38043 Grenoble Cedex, France.

*Present address: Oregon Hearing Research Center and Vollum Institute, Oregon Health and Science University, Portland, OR 97201, USA.
†To whom correspondence should be addressed. E-mail: nicolson@ohsu.edu

Downloaded from www.sciencemag.org on January 2, 2007

Whole-mount in situ hybridizations confirmed that *starmaker* is expressed in the developing ear (Fig. 1, C to F). At very early stages, *starmaker* appears to be expressed by the entire epithelium of the otic placode (Fig. 1, C and D). *starmaker* mRNA is also expressed in the pineal gland, and very weak expression was observed in the tail region (Fig. 1C). During embryonic development, expression of *starmaker* is increasingly restricted to distinct patches of cells representing the sensory epithelium (Fig. 1, E and F). In day 3 larvae, the neuromasts or superficial sensory hair neuroepithelia of the lateral line organ are also labeled (Fig. 1, E and F). In addition, we observed transient and low levels of expression in the eye and nose.

To gain insight into the function of *starmaker*, we injected modified antisense oligonucleotides or "morpholinos" (MOs) into one-cell-stage embryos (*16*). MOs act by interfering with splicing or translation of the message (*17*, *18*). Reduction of *starmaker* activity using a splice site MO (GT-MO) resulted in a severe alteration in otolith morphology (Fig. 2, A to G). With increasing doses of the GT-MO, we observed a change from nearly wild-type otoliths with slightly irregular shapes to star-shaped otoliths and finally to otoliths resembling chunks of pure crystalline calcium carbonate (Fig. 2, D and H). Reverse transcription polymerase chain reaction (RT-PCR) analysis of RNA extracts from injected animals and subsequent sequence analysis of the PCR products showed that the GT-MO caused the removal of exon 16 or retention of intron 16 (Fig. 2I) (*19*). This gave rise to two versions of mutated protein: one lacking the 25 amino acids encoded by exon 16, and the other having a truncation after exon 16 due to a premature stop codon in the intron. Despite the changes in morphology induced by the GT-MO, it was still possible that the otolith phenotypes we saw represented only a hypomorphic situation. To mimic a *starmaker* loss-of-function situation, we used a second MO directed against the translation initiation site (ATG-MO). Injections of low amounts (2 ng) of the ATG-MO led to otoliths resembling clumps of crystals otherwise only obtained with very high doses of GT-MO. In rare cases we also observed star-shaped otoliths. Simultaneous injection of both MOs did not further alter the phenotype. Both MOs appeared to be specific because we did not observe any other obvious morphological defects. Background effects such as small heads or heart edemas were seen only at high doses (40 ng) of MOs (about 15% of all injected animals). Thick sections (10 μm) of neuromasts and the pineal gland did not reveal any gross abnormalities in these organs (*19*). It is notable that *starmaker* is expressed in the neuroepithelia of the semicircular canals and neuromasts, and yet these organs do not contain biomineralized structures. *starmaker* may serve a different function in these tissues.

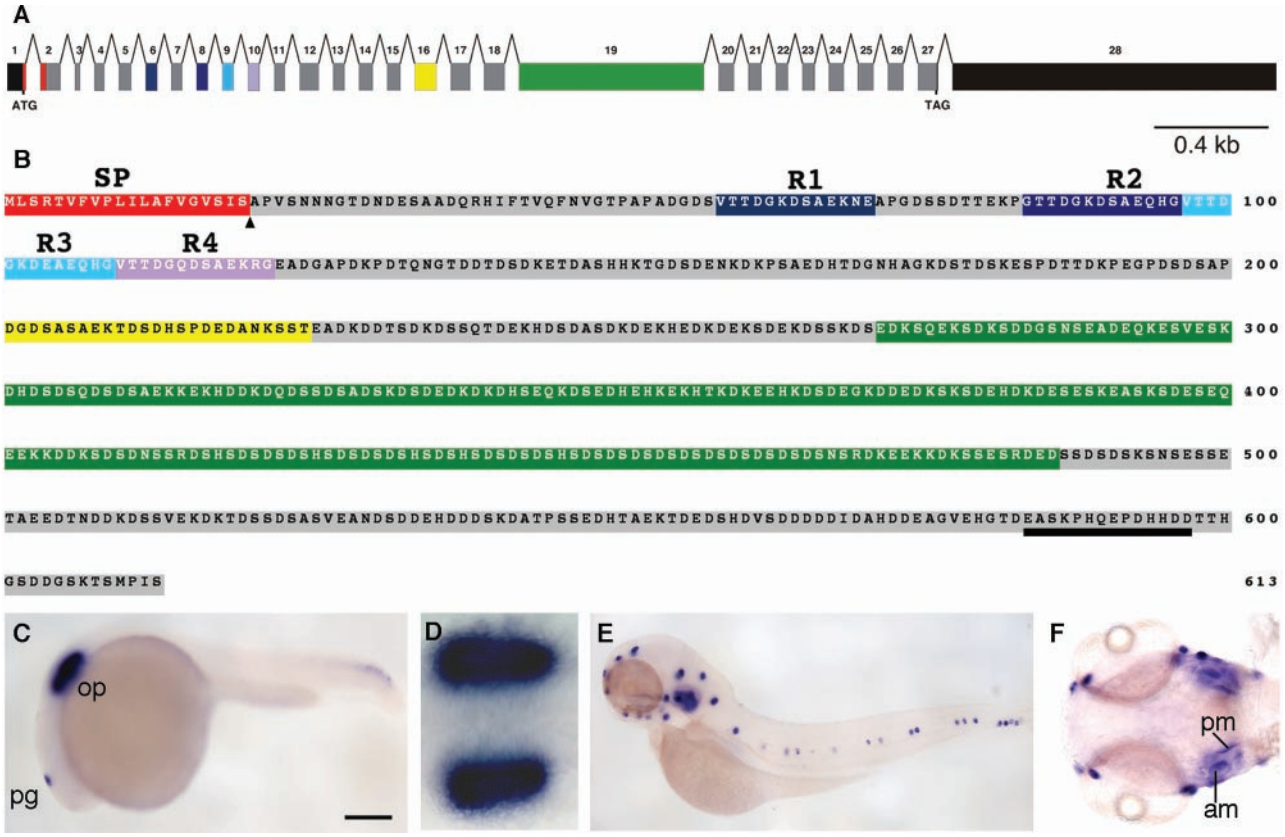


Fig. 1. The *starmaker* genomic structure, predicted amino acid sequence, and mRNA expression pattern during development of zebrafish. (**A**) The *starmaker* gene contains 28 exons. The sizes of the introns are not depicted to scale. (**B**) Structural features of the Starmaker protein. The signal peptide (SP) consists of 20 amino acids. The predicted cleavage site between position 20 and 21 is indicated by an arrowhead. Four highly conserved internal repeats (R1 to R4) depicted in dark blue to violet are present. Each repeat is encoded by a single exon, indicated with an identical color code in (A). The protein part shaded in yellow is deleted via aberrant splicing caused by the GT-MO. Exon 19 (indicated in green) encodes a stretch of mainly serine and aspartic acid residues. A peptide stretch near the C-terminus of the protein (indicated with a black line) was used to generate an antibody. (C to F) Whole-mount mRNA in situ hybridization of *starmaker* mRNA in zebrafish embryos and larvae. (**C**) Lateral view of a 24-hpf embryo. There is strong expression in the developing ear or otic placode and the pineal gland above the eyes. (**D**) Dorsal view of the otic placode at 20 hpf. (**E**) Lateral view of a 72-hpf larva. Expression in clusters of sensory hair cell epithelium (lateral line organ) can be seen along the entire length of the animal. (**F**) Dorsal view of the expression in the larval ear (72 hpf). Expression is mainly restricted to the neuroepithelial patches within the ear. am, anterior macula, op, otic placode, pg, pineal gland, pm, posterior macula. Scale bar in (C) indicates 35 μm in (C), 14 μm in (D), 250 μm in (E) and 125 μm in (F).

Downloaded from www.sciencemag.org on January 2, 2007

The misshapen otoliths caused a behavioral phenotype. The majority of 5-day-old fish injected with either MO had difficulty in orienting themselves quickly in fast moving water in comparison to uninjected larvae. A fraction of these injected or "morphant" larvae (up to 20% with 40 ng MO) also displayed circling behavior typical for fish with vestibular defects. After 10 days, many GT-MO–injected animals swam normally, presumably because the MOs were no longer effective at this late stage. However, none of the ATG-MO–injected animals survived.

The process of otolith formation can be separated into two stages. During the first stage between 18 hours postfertilization (hpf) and 24 hpf, seeding particles attach to the kinocilia of the tether cells, which are located at the anterior and posterior part of the otic placode (*20*, *21*). These seeding particles are composed of glycogen and form the nucleus or the core of the otolith (*22*). After 24 hours, the speed of otolith formation slows down and otoliths start to display a daily growth pattern (*23*). In transmission electron microscope cross sections of wild-type and morphant otoliths, we observed that the core of the otoliths, represented by darkly stained spheres, was always present in the morphants, indicating that the initial step of otolith seeding and anchoring was normal (Fig. 2, E to G). In wild-type otoliths, successive rings of matrix proteins enclose the core (*24*, *25*), and the central part of the surface facing the neuroepithelium is very electron-dense (Fig. 2E). Successive rings are no longer present in the star-shaped otoliths, although it was still possible to detect an electron-dense surface facing the neuroepithelium (Fig. 2F). In the most severely affected otoliths, we observed a dramatic change of the protein skeleton surrounding the otolithic core (Fig. 2G). The fibrous matrix was disorganized and did not run in a radial direction as seen in the less-affected or wild-type otoliths. In addition, the organic matrix was not intercalated within the crystals. Instead, organic matrix was sandwiched between and excluded from single, large, presumably inorganic crystals (Fig. 2G).

The appearance of the most severe form of morphant otolith was fundamentally different from those of the other morphant otoliths. The complexity and cubic faces of the crystals suggested that the polymorph of calcium carbonate was calcite rather than aragonite. To determine which crystal polymorph was present in each type of otolith, we performed x-ray microdiffraction experiments at the ID13 beamline of the European Synchtron Radiation Facility–Grenoble (*16*, *26*). The diffraction patterns obtained from wild-type otoliths confirmed that they were composites of small crystallites with the crystal lattice of aragonite (Fig. 3, A to C). The same result was obtained with the intermediate type of otoliths (19). The polymorph present in the star-shaped otoliths was also aragonite (Fig. 3, D and F). In contrast, the x-ray diffraction pattern of the most severely affected otoliths showed a switch in their crystal habit or polymorph from aragonite to calcite (Fig. 3, G and I). In addition, the averaged diffraction patterns showed a change in texture. In wild-type and star-shaped otoliths, the diffraction patterns showed Debye rings, indicating the presence of many crystallites with dimensions smaller than the beam size (Fig. 3, B and E). However, the grainy pattern in Fig. 3E suggests that the crystallites in the star-shaped otoliths are bigger than normal. In contrast to the above patterns, the Debye rings of the calcitic otoliths diffraction patterns were spotty, indicating that they are composed of a small number of grains with dimensions larger than the beam size (Fig. 3H). In the absence of Starmaker, the formation of the large calcite crystals may represent a "default" situation in which the more stable of the two polymorphs, calcite, is favored.

To determine whether Starmaker was physically located at the site of crystal formation, we generated a C-terminal antibody for immunolocalization. With the use of Western blot analysis, we detected a single band that was reduced in morphants (fig. S1). In 24-hpf larvae, antibody (Ab) against Starmaker labeled both anterior and posterior otoliths and the apical surface of the epithelial cells of the otic placode (Fig. 4A). At this early stage, many small particles floating in the lumen of the ear were labeled (Fig. 4B). These particles most likely represent otolith seeding particles. At later stages (day 5), the surface of both anterior and posterior otoliths was still labeled (Fig. 4E). In addition, we detected labeling in neuromasts (fig. S1). In ultrathin cross sections stained with Starmaker Ab, we saw labeling of the apical surfaces of the neuroepithelium [counterstained with the nuclear marker 4′,6′-diamidino-2-phenylindol (DAPI)] and both external and internal labeling of otoliths (Fig. 4, C and D). Labeling was particularly strong along the flat surface of the otolith (Fig. 4C). In larvae injected with the GT-MO, the staining was reduced but still present at the

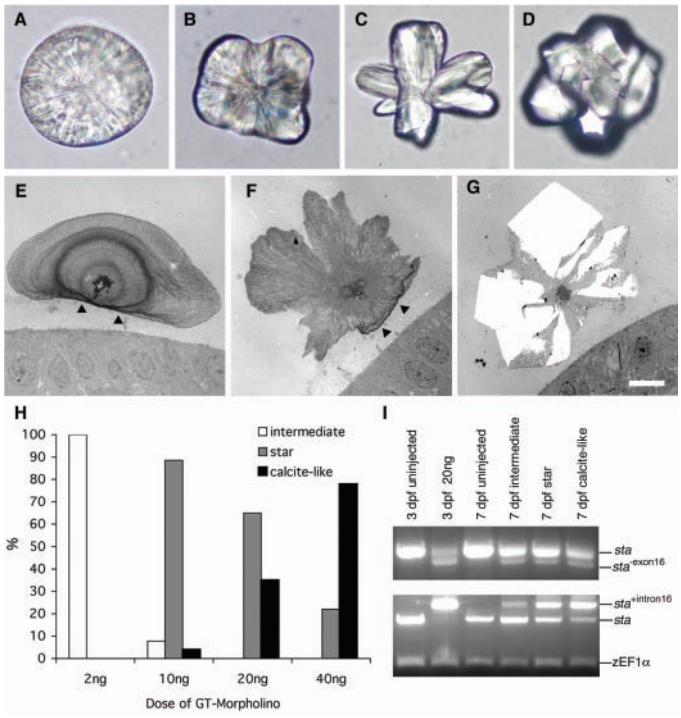


Fig. 2. Reduction of *starmaker* activity alters otolith morphology in zebrafish. (A to D) Isolated single otoliths from uninjected and GT-MO–injected fish (day 7). Bright-field images of (**A**) wild-type, (**B**) intermediate (2 ng), (**C**) star-shaped (20 ng), and (**D**) calcite-like (40 ng) otoliths. (E to G) Transmission electron microscope cross sections of otoliths from 5-day-old fish. (**E**) Wild-type otolith. The center consists of darkly stained spheres and is surrounded by successive rings of fibrous matrix material. The characteristic shape is oval with a flat surface (arrowheads) facing the neuroepithelium. (**F**) Star-shaped otolith. The successive rings of fibrous matrix are absent. (**G**) The most severe form (calcite-like). The fibrous matrix is reduced and excluded from regions that appear to be pure crystal. Scale bar in (G) indicates 13 μm in (A) to (D) and 10 μm in (E) to (G). (**H**) Dose response curve for the GT-MO. For each concentration, a total of 140 otoliths have been examined in three separate experiments (day 4, $n = 35$ larvae). (**I**) The GT-MO directed against a donor splice site causes removal of exon 16 or retention of intron 16. The efficiency of the reduction in 3-day-old fish is still quite high. In day 7 fish, there is a strong correlation between the increase of the severity of the phenotype and reduction of the *starmaker* wild-type message. The RT-PCR experiments were carried out with the use of pools of five larvae. The upper gel shows PCR products obtained with the use of a shorter extension time than the lower gel. As a control, we used zebrafish *elongation factor 1*α primers.

Downloaded from www.sciencemag.org on January 2, 2007

outer edges of the otoliths (Fig. 4F). In contrast, Starmaker Ab did not label the otoliths in ATG morphants (Fig. 4, G and H). This result indicates that the ATG-MO was very effective in limiting expression of *starmaker*, and the reduction of staining in both GT and ATG morphants demonstrates the specificity of the C-terminal antibody. Our immunolocalization results indicate that the protein is secreted into the lumen of the ear and is an organic component of the otolith.

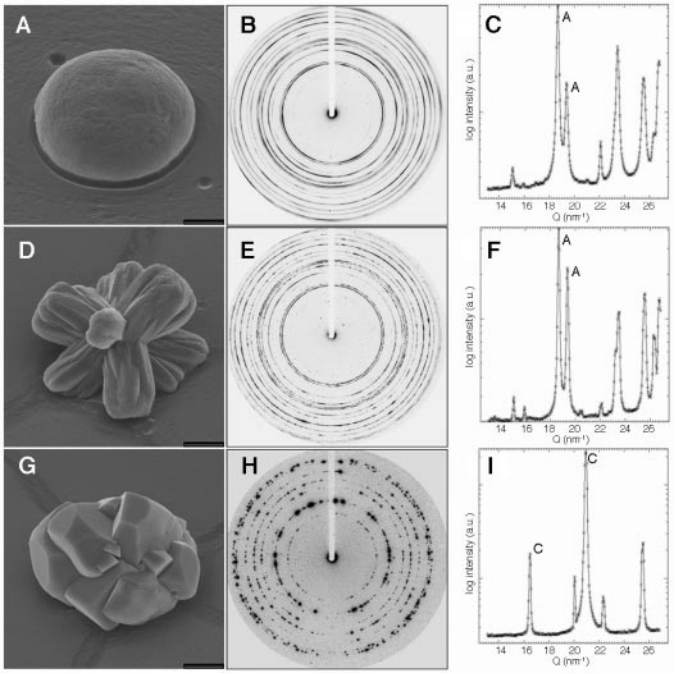


Fig. 3. Determination of the crystal habit and properties in wild-type and morphant otoliths (day 7) using x-ray diffraction analysis. (**A**) Scanning electron micrograph of a wild-type otolith with an averaged x-ray diffraction pattern (**B**) obtained with a 5-μm beam (wavelength of $\lambda = 0.09745$ nm). The otolith was rotated 180° to sample all crystalline orientations. The Debye rings do not show a preferred orientation. (**C**) One-dimensional intensity distribution as a function of Q ($Q = 2p/d$ where d is the lattice spacing) obtained by azimuthally averaging the wild-type otolith pattern shown in (B). The strongest peaks identify the calcium carbonate polymorph as aragonite (marked with "A"). a.u., arbitrary units. (**D** to **F**) Micrograph of a star-shaped otolith and the corresponding diffraction pattern and Q-dependent intensity distribution. The rings (E) are slightly grainier than those in wild-type otoliths, but aragonite is still present (F). (G to I) Most severe form resembling pure crystals. (**G**) The morphology of the crystals is characteristic of calcite. (**H**) The averaged diffraction pattern shows spotty Debye rings, indicative of large grains of calcite. (**I**) Transition from aragonite to calcite (strongest calcite peaks marked with "C"). Scale bars in (A), (D), and (G), 20 μm.

In vitro studies with mollusk shells have suggested that acidic proteins extracts have the ability to control nucleation and growth of calcium carbonate crystals on an appropriate framework of matrix macromolecules. Moreover, the control of crystal habit formation is dependent upon the presence of these polyanionic protein extracts (*27–29*). In our study, we observed a similar effect: a switch in calcium carbonate polymorph in the absence of Starmaker. Regularly spaced acidic groups in peptides forming β sheets can serve as a template for the binding of divalent ions, leading to the formation of crystals (*30*). The repeating series of alternating serines and aspartic acids in Starmaker is predicted to form β sheets and may thus serve as a template for nucleation, selecting aragonite over calcite.

The acidic nature and localization of Starmaker, along with its spatial and temporal expression patterns, point at a possible mechanism for otolith biomineralization. Restricted localization of Starmaker at later stages of development demonstrates that it is more concentrated at the surface of the otolith facing the sensory epithelium than at the opposite surface. Bound Starmaker may act by inhibiting or regulating crystal growth mainly at this surface, giving rise to the flat-bottom shape of the otolith (Fig. 2E). In support of this notion, we observe a greater density of fibrous organic material at this surface at the electron-microscope level. In morphant calcitic otoliths, this electron-dense material is absent, and it is no longer possible to distinguish whether a surface was facing the

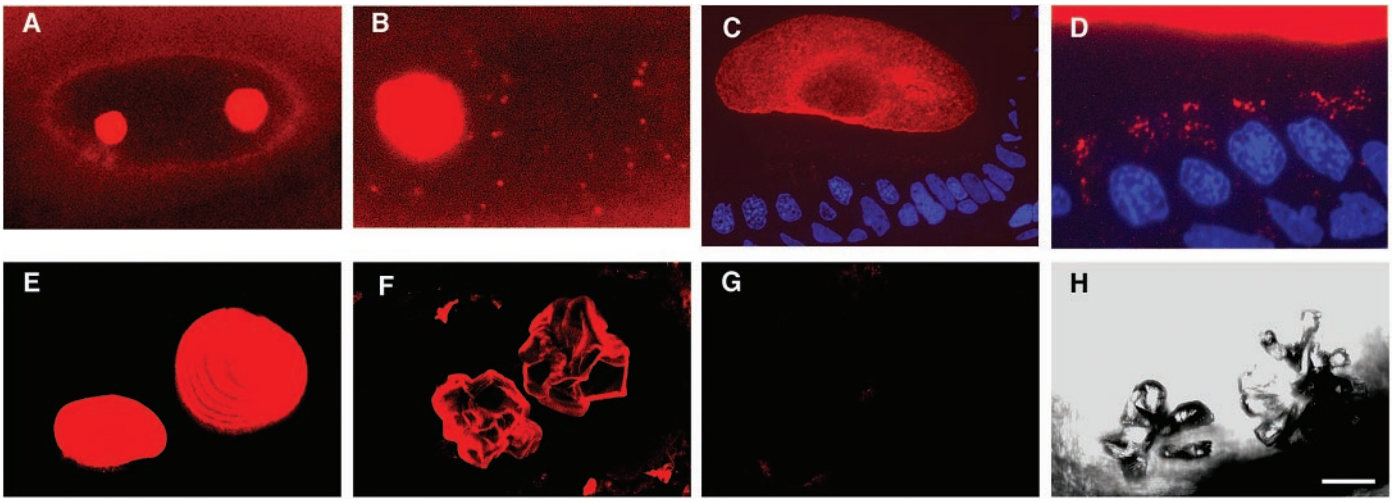


Fig. 4. Starmaker localizes to otoliths. Whole mounts [(A), (B), and (E) to (H)] or ultrathin sections (70 nm) [(C) and (D)] were labeled with a C-terminal antibody against Starmaker. (**A**) Lateral view of an embryonic ear at 24 hpf. (**B**) Higher magnification of the floating seeding particles in the lumen. (C and D) Ultrathin sections labeled with anti-Starmaker antibody and counterstained with DAPI (day 5). (**C**) Surface and internal labeling of the otolith. Note the stronger signal along the flat surface facing the epithelium. (**D**) Labeling at the apical surface of the neuroepithelium is also detectable. (E to H) Confocal images (multiple optical sections) of otoliths in uninjected and injected fish (day 5). (**E**) Strong labeling of both otoliths in an uninjected wild-type larva. (**F**) Reduction of labeling in a larva injected with GT-MO (20 ng). (**G**) Absence of labeling in a larva injected with ATG-MO (20 ng). (**H**) Bright-field image of the otoliths in (G). Scale bar in (H) indicates 5 μm in (A) and (C), 2 μm in (B) and (D), and 30 μm in (E) to (H).

Downloaded from www.sciencemag.org on January 2, 2007

neuroepithelium on the basis of its shape.

The role of Starmaker in otolith morphogenesis presents an interesting example of a biological influence on the process of crystallization. In particular, Starmaker is crucial for crystal polymorph selection and thus provides a molecular handle for exploring this intriguing interface between biology and mineral formation.

References and Notes

1. H. A. Lowenstam, *Science* **211**, 1126 (1981).
2. H. A. Lowenstam, S. Wiener, *On Biomineralization* (Oxford Univ. Press, Oxford, 1989).
3. G. Borelli, N. Mayer-Gostan, H. De Pontual, G. Boeuf, P. Payan, *Calcif. Tissue Int.* **69**, 356 (2001).
4. S. E. Campana, *Mar. Ecol. Prog. Ser.* **188**, 263 (1999).
5. R. R. Fay, *Science* **225**, 951 (1984).
6. A. Popper, C. Platt, *Inner Ear and Lateral Line. In the Physiology of Fishes* (CRC Press, Boca Raton, FL, 1993), pp. 99–136.
7. K. Pote *et al.*, *Biochemistry* **32**, 5017 (1993).
8. E. Verpy, M. Leibovici, C. Petit, *Proc. Natl. Acad. Sci. U.S.A.* **96**, 529 (1999).
9. Y. Wang *et al.*, *Proc. Natl. Acad. Sci. U.S.A.* **95**, 15345 (1998).
10. L. Everett *et al.*, *Hum. Mol. Genet.* **10**,153 (2001).
11. B. Hurle *et al.*, *Hum. Mol. Genet.* **12**, 777 (2003).
12. S. Xiao *et al.*, *Nature Genet.* **27**, 201 (2001).
13. X. Zhang *et al.*, *Nature Genet.* **27**, 151 (2001).
14. The biomineral in teeth is composed of calcium phosphate as opposed to calcium carbonate, which is present in otoconia.
15. N. Blom, S. Gammeltoft, S. Brunak, *J. Mol. Biol.* **294**, 1351 (1999).
16. Information on materials and methods is available on *Science* Online.
17. A. Nasevicius, S. C. Ekker, *Nature Genet.* **26**, 216 (2000).
18. B. W. Draper, P. A. Morcos, C. B. Kimmel, *Genesis* **30** 154 (2001).
19. C. Söllner *et al.*, data not shown.
20. B. B. Riley, C. Zhu, C. Janetopoulos, K. J. Aufderheide, *Dev. Biol.* **191**, 191 (1997).
21. C. Haddon, J. Lewis, *J. Comp. Neurol.* **365** 113 (1996).
22. M. Pisam, C. Jammet, D. Laurent, *Cell Tissue Res.* **310**, 163 (2002).
23. G. Pannella, *Science* **173**, 1124 (1971).
24. R. L. Radtke, J. M. Dean, *Fish. Bull.* (*Dublin*) **80**, 201 (1982).
25. J. D. Neilson, G. H. Green, B. Chan, *Fish. Bull.* (*Dublin*) **83**, 81 (1985).
26. C. Riekel, *Rep. Prog. Phys.* **63**, 233 (2000).
27. S. Weiner, L. Addadi, *Trends Biochem. Sci.* **16**, 252 (1991).
28. G. Falini, S. Albeck, S. Weiner, L. Addadi, *Science* **271**, 67 (1996).
29. A. M. Belcher *et al.*, *Nature* **381**, 56 (1996).
30. J. H. F. Haimanot Bekele, J. W. Kelly, *J. Am. Chem. Soc.* **121**, 7266 (1999).

31. We thank J. Ihringer and T. Wenzel for helpful suggestions, A. Lupas for advice, and S. Sidi and C. Seiler for helpful comments on the manuscript. Supported by funding from the Max Planck Society, Sonderforschungsbereich 430, and the Deutsche Forshungsgemeinschaft (NU 22/5-1).

Supporting Online Material

www.sciencemag.org/cgi/content/full/302/5643/282/DC1
Materials and Methods
Fig. S1
References and Notes

25 June 2003; accepted 27 August 2003

A Functional Link Between RuBisCO-like Protein of *Bacillus* and Photosynthetic RuBisCO

Hiroki Ashida,[1] Yohtaro Saito,[1] Chojiro Kojima,[1] Kazuo Kobayashi,[1] Naotake Ogasawara,[1] Akiho Yokota[1,2]*

The genomes of several nonphotosynthetic bacteria, such as *Bacillus subtilis*, and some Archaea include genes for proteins with sequence homology to the large subunit of ribulose bisphosphate carboxylase/oxygenase (RuBisCO). We found that such a RuBisCO-like protein (RLP) from *B. subtilis* catalyzed the 2,3-diketo-5-methylthiopentyl-1-phosphate enolase reaction in the methionine salvage pathway. A growth-defective mutant, in which the gene for this RLP had been disrupted, was rescued by the gene for RuBisCO from the photosynthetic bacterium *Rhodospirillum rubrum*. Thus, the photosynthetic RuBisCO from *R. rubrum* retains the ability to function in the methionine salvage pathway in *B. subtilis*.

Ribulose 1,5-bisphosphate carboxylase/oxygenase (RuBisCO), the most abundant naturally occurring protein (*1*), functions in the Calvin cycle during photosynthesis to convert atmospheric CO_2 into organic carbon. RuBisCO has several disadvantages as a biological catalyst. Besides having a low affinity for the substrate CO_2 and a low turnover rate, its CO_2-fixation activity is competitively inhibited by O_2 (*2*, *3*). To overcome these disadvantages, plants are obliged to invest a large amount of nitrogen to synthesize adequate levels of RuBisCO. The disadvantages may reflect the molecular evolution of RuBisCO when the Calvin cycle appeared; however, the ancestral gene remains to be identified.

RuBisCOs and proteins with sequence similarity are classified into four forms (Fig. 1A): The enzyme that is most strongly adapted to present-day atmospheric conditions represents form I, which consists of eight large and eight small subunits. It is found in photosynthetic organisms such as higher plants, algae, and autotrophic proteobacteria. Form II, with the simplest structure, is found in some photosynthetic bacteria, such as *Rhodospirillum rubrum* (*4*). Form III consists of the large subunits only, and it is found in some Archaea (*5*, *6*). Forms I through III include the amino acid residues that are required for catalytic activity of RuBisCO, and each is capable of catalyzing both the carboxylation and the oxygenation of ribulose-1,5-bisphosphate (RuBP). Form IV has been found in *Bacillus subtilis* (*7*), *Chlorobium tepidum* (*8*, *9*), and *Archaeoglobus fulgidus* (*10*). It lacks several of the amino acid residues involved in catalysis (*8*) (Fig. 1B). Forms III and IV are referred to as RuBisCO-like proteins (RLPs). Their functional and evolutionary relation to photosynthetic RuBisCO are unknown. We describe the functional relation between a RuBisCO-like protein of *B. subtilis* and photosynthetic RuBisCO.

The *ykrW* gene for the RLP of *B. subtilis* is the first gene in the *ykrWXYZ* operon, which is close to the *ykrTS* operon (*7, 11–13*). These operons have S-box presequences that regulate the expression of the genes involved in sulfur metabolism in *B. subtilis* (*11*, *12*), and it has been predicted that the genes in these operons are involved in the methionine salvage pathway (*11*, *13*). In this pathway, organic sulfur is salvaged from methylthioribose (MTR), which is derived from the methylthioadenosine (MTA) that is a by-product of the synthesis of spermidine. In the pathway that has been proposed in *Klebsiella pneumoniae* (*14–18*) (fig. S1), MTR is phosphorylated to MTR-1-phosphate (MTR-1-P) by a kinase, and then MTR-1-P is isomerized by an aldose-ketose isomerase to methylthioribulose-1-phosphate (MTRu-1-P). MTRu-1-P then undergoes a dehydration reaction that is catalyzed by a dehydratase and yields 2,3-diketo-5-methylthiopentyl-1-phosphate (DK-MTP-1-P). DK-MTP-1-P is converted to 1,2-dihydroxy-3-keto-5-methylthiopentene (DHK-MTPene) via the intermediate, 2-hydroxy-3-keto-5-methylthiopentenyl-1-phosphate (HK-MTPenyl-1-P), by an enolase/phosphatase. Finally, DHK-MTPene is converted to formate and 2-keto-4-methylthiobutyrate (KMTB) by a dioxygenase, and KMTB is transaminated to methionine.

[1]Graduate School of Biological Sciences, Nara Institute of Science and Technology (NAIST), 8916-5 Takayama, Ikoma, Nara 630-0101, Japan. [2]Plant Molecular Physiology Laboratory, Research Institute for Innovative Technology for the Earth (RITE), 9-2 Kizugawadai, Kizu, Sorakugun, Kyoto 619-0292, Japan.

*To whom correspondence should be addressed. E-mail: yokota@bs.aist-nara.ac.jp

Downloaded from www.sciencemag.org on January 2, 2007